Global propagation of ionospheric disturbances associated with the 2022 Tonga Volcanic Eruption

David R. Themens[1,2], Chris Watson[2], Nedjeljka Žagar[3], Sergiy Vasylkevych[3], Sean Elvidge[1], Anthony McCaffrey[2], Paul Prikryl[2], Ben Reid[2], Alan Wood[1], and P.T. Jayachandran[2]

1) Space Environment and Radio Engineering Group (SERENE), University of Birmingham, Birmingham, UK

2) Department of Physics, University of New Brunswick, Fredericton, NB, Canada

3) Meteorologisches Institut, Universität Hamburg, Hamburg, Germany

Abstract

In this study, we use measurements from over 4,735 globally distributed Global Navigation Satellite System (GNSS) receivers to track the progression of travelling ionospheric disturbances (TIDs) associated with the 15 January 2022 Hunga Tonga-Hunga Ha'apai submarine volcanic eruption. We identify two distinct Large Scale TIDs (LSTIDs) and several subsequent Medium Scale TIDs (MSTIDs) that propagate radially outward from the eruption site. Within 3000 km of epicenter, LSTIDs of >1600 km and ~1350 km wavelengths are initially observed propagating at speeds of ~950 ms^{-1} and ~555 ms^{-1}, before substantial slowing to ~600 ms^{-1-} and ~390 ms^{-1}, respectively. MSTIDs with speeds of 200-400 ms^{-1} are observed for six hours following eruption, the first of which comprises the dominant global ionospheric response and coincides with the atmospheric surface pressure disturbance associated with the eruption. These are the first results demonstrating the global impact of the Tonga eruption on the ionospheric state.

Key Points:

1) Highly directional LSTIDs are generated from the Tonga Eruption at initial speeds up to 950 m/s and propagate potentially as far as 20,000km.
2) Outside the local area of the eruption, MSTIDs coincident with the surface pressure wave form the dominant ionospheric response.
3) Secondary MSTIDs continue to be produced in the vicinity of the eruption for up to 6 hours following the event.

Plain-Language Summary

The 2022 Tonga oceanic volcanic eruption and resulting tsunami was an incredibly impulsive and high energy event. Such events can generate strong pressure waves in the atmosphere that can propagate up into the Earth's ionosphere and modulate the plasma therein. Using every available Global Navigation Satellite System (GNSS) receiver from a global network of over 4,735 instruments, we were able to track the propagation of these waves from the Tonga eruption site around the planet. We show that an initial shock front at speeds up to 950 ms^{-1} strongly perturb the ionospheric electron density near the eruption site and within a narrow extended region to the North, while smaller, slower waves originating from the eruption make up the strongest ionospheric response at distances far away from the eruption region. Small scale ionospheric waves continue to be produced near the eruption for up to six hours after the eruption began. These waves were tracked from the eruption to over 20,000km from the epicenter and could very well have persisted beyond the one day studied here.

Introduction

Volcanic eruptions, earthquakes, atmospheric convective systems, and tsunamis have long been shown to invoke measurable ionospheric wave responses that can travel thousands of kilometers [Heki 2006; Dautermann et al., 2009; Tsugawa et al., 2011; Komjathy et al., 2012; Nishioka et al., 2013; Chou et al., 2017; Chen et al., 2017; Savastano et al., 2017; Inchin et al., 2020]. The acoustic and gravity waves (AGWs) and Rayleigh waves (RWs) resulting from these disturbances in the lower atmosphere and ocean [Mayr et al., 1984a; 1984b] can form traveling ionospheric disturbances (TIDs). These TIDs can cause minor perturbations in the integrated electron density of the ionosphere [Dautermann et al., 2009; Komjathy et al., 2016] and, in more severe cases, significant ionospheric tilting that has substantial implications for radio propagation at High Frequencies (HF) due to off-great circle propagation [Zawdie et al., 2016; Cervera and Harris, 2014]. With Global Navigation Satellite Systems (GNSS) we can track the progression of these waves in near real time [Savastano et al., 2017] and may soon provide operators with corrections necessary to ensure the resiliency of their systems to TID effects. In this study, we investigate the progression of TIDs as they circumnavigate the globe following the Hunga Tonga-Hunga Ha'apai (herein simply referred to as Tonga) underwater volcanic eruption and associated tsunami in January 2022.

Previous studies of the 2011 Tohoku earthquake and tsunami showed the generation of fast (3457 ms^{-1}) concentric Large Scale Traveling Ionospheric Disturbances (LSTIDs) associated with an RW that quickly dissipated at ranges of ~1000 km from the source, followed by Medium Scale TIDs with velocities in the range of 138-423 ms^{-1} [Tsugawa et al., 2011]. Savastano et al. [2017] demonstrated the real time tracking of earthquake and tsunami-related ionospheric disturbances, finding wave propagation speeds of 316 ms^{-1} for ionospheric structures induced by

the 2012 Haida Gwaii earthquake, consistent with the acoustic speed. More recently, Inchin et al. [2020] and Zettergren and Snively [2019] used sophisticated atmospheric wave propagation modeling to explore the causes and behavior of earthquake-induced TIDs and demonstrated considerable non-linear effects and a high degree of anisotropy in the propagation of AGWs and RWs associated with earthquakes.

Unfortunately, due to observational limitations most studies rarely examine the global impact of such events. To examine whether the global coverage GNSS observational capacity and the sheer impulsive size of this event would allow us to track these structures from production to dissipation, we have here gathered data from every public GNSS receiver network available to the authors and explore the behavior of ionospheric TIDs generated by the Tonga volcanic eruption that began at 04:15 UT January 15 2022, centered at (20.546^{o}S, 175.390^{o}W) (https://earthquake.usgs.gov/earthquakes/eventpage/pt22015050/origin/detail).

Data

GNSS measurements have long represented a vital dataset in the study of the global ionospheric response to a wealth of phenomena. Using measurements of carrier phase and code pseudorange on a pair of UHF signals, the integrated electron density of the ionosphere can be found [Themens et al., 2013]. One can relate the integrated electron density along the GNSS ray path, i.e. the Total Electron Content (TEC), to the phase difference on two signals via the following

$$sTEC = \frac{1}{A}\left(\frac{f_1^2 f_2^2}{f_1^2 - f_2^2}\right)(\Delta L + W + rDCB + sDCB)\#(1)$$

where A = 40.3, f_i is the first or second signal frequency, ΔL is the carrier phase difference between the two signals, W is a phase leveling parameter used to correct phase cycle ambiguities with code measurements, *rDCB* is the receiver Differential Code Bias (DCB), and *sDCB* is the satellite DCB. For this study, we make use of only Global Positioning System (GPS) constellation measurements in the L1 C/A - L2P combination. To take advantage of the exceptional precision of carrier phase measurements, one would generally "phase level" the carrier TEC to that from the code pseudorange measurements using a satellite elevation weighting, as in Themens et al. [2013]. In this study, we are interested solely in the relative variations in TEC, which are typically calculated by applying a high-pass filter to un-leveled, un-bias-corrected slant TEC (sTEC) [Komjathy et al., 2012; Zhang et al., 2019]. This approach, however, can lead to an elevation dependence in the amplitude of variations due to the slant propagation path. To mitigate this potential artifact, we instead opt to level our phase sTEC measurements to pseudorange sTEC, apply satellite bias estimates from the Center for Orbit Determination (CODE) (ftp://ftp.aiub.unibe.ch/), and then apply the Ma and Maruyama [2003] receiver bias estimation method to get a first-order estimate of the absolute TEC. By removing biases and phase-leveling, we can project the sTEC to vertical TEC (vTEC) using the standard thin ionospheric shell model with a shell height of 400 km [Themens et al., 2015] without also imposing a significant projection function-dependent trend to the vTEC [Themens et al., 2015].

This vTEC is then detrended by removing the 30-minute-wide, boxcar smoothed vTEC from the unsmoothed vTEC, which is consistent with what has been used previously in studies of the global propagation of MSTIDs and Large-Scale TIDs (LSTIDs) in Zhang et al. [2019];

however, as noted in Coster et al. [2017], the length of the chosen detrending window can have an impact on the characteristics of the residual waves. Use a detrending window that is too wide and you risk introducing substantial trends from quiescent ionospheric variability and masking smaller scale structures behind stronger large-scale variability. Use a detrending window that is too narrow and you risk removing parts of the desired signal. In our case, we sit on the boundary of these two scenarios, where we have both LSTIDs and MSTIDs of interest. Using the 30-minute window will allow us to easily identify the MSTIDs, but may artificially suppress the observed amplitude of LSTID structures.

To further ensure the reliability of the data, any intervals with missing data, such as partial intervals at the start of arcs of lock or across cycle slip events are omitted to ensure the consistency of the smoothing interval and mitigate the impact of some cycle slips. Accounting for DCBs may be an unnecessary step as the detrending process would remove slow moving trends imposed by erroneous DCB projections, but we still apply DCB corrections as a precautionary measure. To limit the amount of horizontal smearing by oblique ray paths, a lower elevation limit of 40 degrees is used.

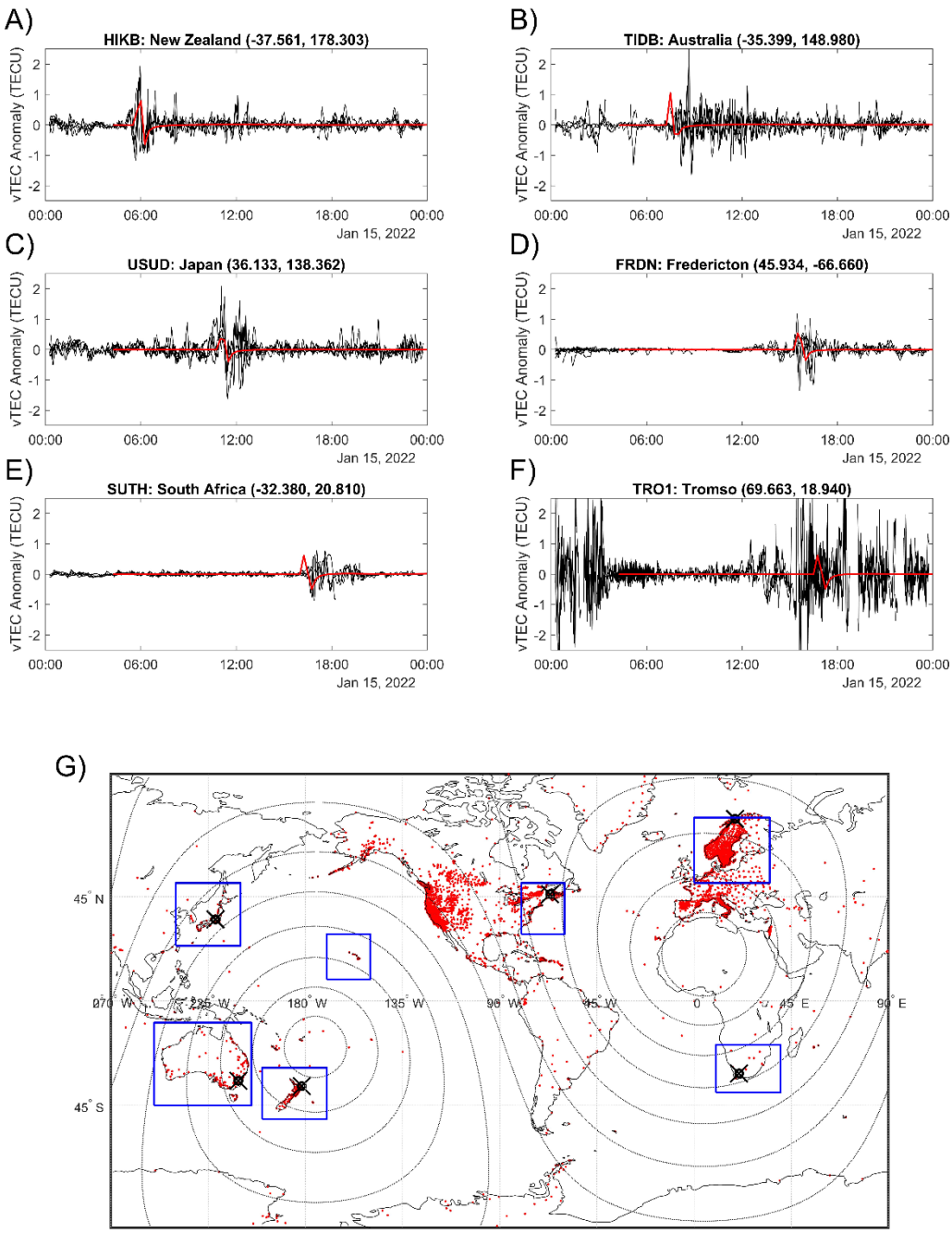

139

140 ***Figure 1.*** *Examples of vTEC anomalies (black) and shallow water layer thickness anomaly in units of*
141 *0.01 meters (red) for stations in New Zealand (A), Australia (B), Japan (C), Peru (D), Eastern Canada*
142 *(E), and South Africa (F). Panel G: Map of GNSS receiver stations used in this study (red). The locations*
143 *of the stations in (A)-(F) are marked with black 'x' symbols. Lines of constant distance from the eruption*
144 *epicenter in 1,500km steps are presented as dotted lines. Blue boxes correspond to the domains used for*
145 *the analysis in Figure 4.*

146

An example of the detrended vTEC at several stations in New Zealand (A), Australia (B), Japan (C), Eastern Canada (D), South Africa (E), and Northern Europe (F) is presented in Figure 1. To track the propagation of these waves globally, we have gathered data from 4,735 distributed GNSS receivers from dozens of local and global receiver networks. These stations correspond to all public data that were available within two days of the eruption. A map of the stations used is presented in Figure 1G, with the sample stations from Figure 1A-F marked with crosses.

The aforementioned processing is applied to each receiver, the ionospheric pierce points (IPPs) of the TEC measurements are calculated using the rapid precise GPS orbits provided by the Crustal Dynamics Data Information System (CDDIS) (https://cddis.nasa.gov/archive/gnss/products/), and the resulting geolocated vTEC perturbations are mapped for the entire day of January 15, 2022. The resulting vTEC measurements are then plotted on maps according to their IPP location for every minute of the day. Example maps and videos of vTEC anomalies are provided in the supplementary material.

To compare the propagation of the ionospheric waves to those at the surface, a barotropic version of the TIGAR (Transient Inertia Gravity and Rossby wave dynamics) model has been run at T170 horizontal resolution. TIGAR solves primitive equations on the sphere using the Hough harmonics [Vasylkevych and Žagar, 2021] thereby providing the time evolution of Rossby and inertia-gravity waves. The atmospheric response to the Tonga eruption is simulated using a homogeneous background (i.e. isothermal and with no winds). The eruption is represented by a Gaussian perturbation at the location of the eruption superimposed on the barotropic atmosphere with a mean depth of 10,114 km. The simulated horizontally-propagating gravity waves represent the Lamb wave in the hydrostatic, isothermal atmosphere. The mean

depth and the parameters of the source were chosen to fit the observed horizontal structure of the eruption and the observed amplitude and timing of surface pressure perturbations.

One method to look at the global propagation of ionospheric disturbances induced by a known source is to organize the vTEC anomalies according to their distance from the source, as in Chen et al. [2017] to characterize earthquake-driven ionospheric TIDs. By binning all vTEC anomalies with latitudes between 55^{o}S and 55^{o}N in 50km bins with respect to radial distance from the eruption location, we can isolate coherent structures associated with the event. We have focused here on regions below 55^{o} since the high degree of other activity at the poles significantly complicates the identification of waves. This approach is applied in Figure 2A, where we see several strong vTEC anomaly structures fanning out from the eruption epicenter (y-axis) and from the time of eruption onset (x-axis). Note that the color scale has been saturated at 0.2 TECU to make wave features easier for the reader to see. Wave amplitudes should instead be inferred from individual station measurements to avoid attenuation/smearing from data binning. Also plotted in Figure 2a, is a superposition of the radial propagation of the pressure disturbance originating from the eruption. This pressure wave propagates at 315 ms^{-1} and is coherent with the generation and propagation of primary MSTIDs from the event.

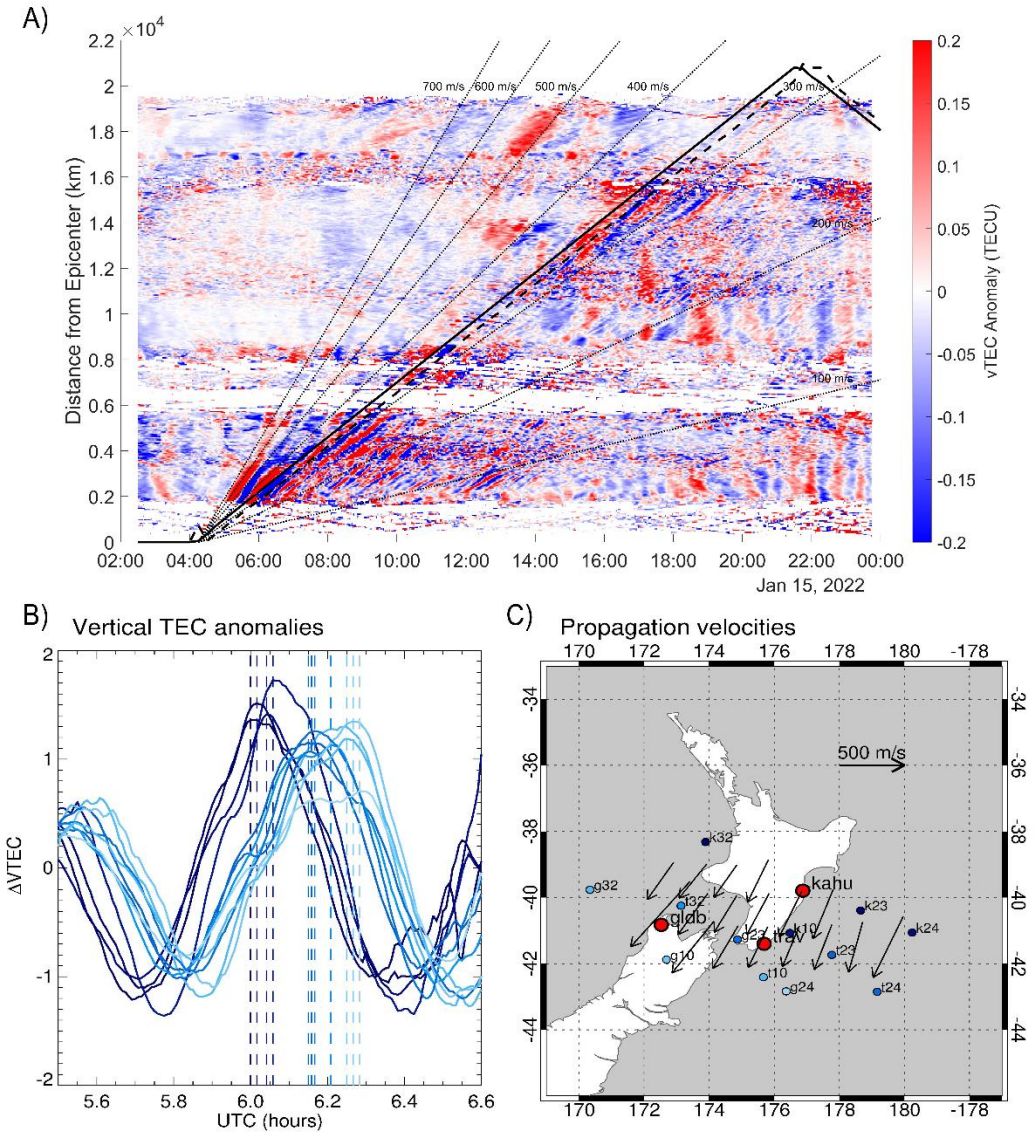

Figure 2. A) *vTEC anomaly averaged in 100km bins of radial distance from the Tonga eruption epicenter. The barotropic model height anomaly peak and depression are plotted in solid and dashed black lines. Dotted black lines correspond to trajectories for fixed radial speeds from 100 ms^{-1} to 700 ms^{-1} in increments of 100 ms^{-1}.* ***B)*** *Demonstration of perturbation front tracking used to determine the velocity estimates in C for a subset of New Zealand stations.* ***C)*** *Demonstration of the velocity estimates (arrows) determined using the triangulation method for a subset of three New Zealand stations. Colored blue dots are IPP locations at time of VTEC anomaly maximum.*

To assess the speed of the disturbances propagating from the eruption event, we use two main methods. The first method is to use triangulation of the irregularities from neighboring

GNSS raypaths. If the TEC signature of a travelling ionospheric disturbance is detected along at least three GPS satellite-receiver raypaths in a localized region, the relative detection time and corresponding IPP locations can be used to estimate the propagation velocity. This method assumes the disturbance has a uniform structure perpendicular to the direction of propagation and requires the assumption of an IPP altitude (400 km), if the altitude of the disturbance is unknown. This TEC triangulation technique has been previously applied in estimating the velocities of ionospheric structures associated with magnetospheric substorms [Watson et al., 2011] and ultra-low frequency magnetic field pulsations [Watson et al., 2015].

The second method for characterizing the wave propagation speed is to trace the slope of coherent wave structures in plots of the distance from the epicenter vs time, such as is presented in Figure 2A. One can then use the fitted slope for each independent structure as an estimate of the propagation speed. Separate point populations are used if a coherent wave structure exhibits a break in its slope, such as was seen in Figure 3A at 2200-2300 km before 06:00UT. A demonstration of the result of both speed estimation methods is presented in Figure 3B-C for the regional domain around New Zealand. Using the derived speeds we can also determine an approximate wave generation time by extrapolating the fitted linear trends to zero range. This implied initiation time is used as the x-axis in Figure 3C, not to be confused with the times in Figure 3A-B. Similarly, the triangulated speeds for each wave front can also be averaged and mapped backward to estimate their implied time of origin. Both approaches are done separately for ranges within and beyond 2300 km to highlight the change in phase speed of the waves with radial distance from the epicenter.

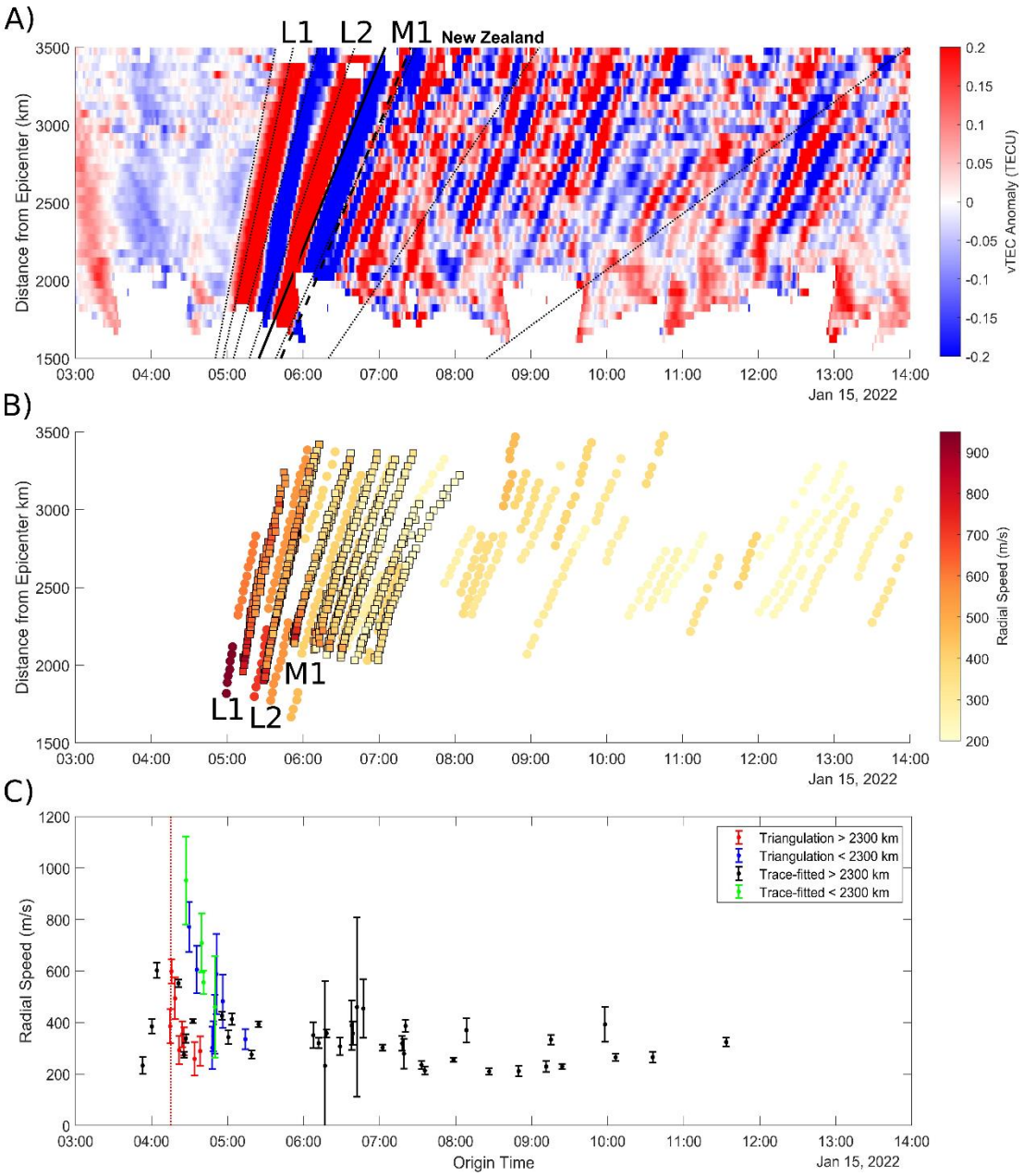

220

221 ***Figure 3. A)*** *Same as Figure 2A, but only using data from within the New Zealand regional domain,*
222 *marked in Figure 1G.* ***B)*** *Traces of the leading and trailing null points of TID signatures from panel A*
223 *colored by the fitted wave speed (circles), and radial distance and time of speed estimates of the*
224 *triangulation method (squares).* ***C)*** *Average wave front speeds corresponding to the New Zealand*
225 *regional domain plotted against estimated time of origin. The beginning of the eruption is marked with a*
226 *vertical red dashed line. Speeds are color coded according to estimation method and radial distance.*

227

228

Results and Discussion

In Figure 1A-F, we see a number of wave packets arriving at sample GNSS receivers at roughly the time of the surface pressure anomaly, with the largest amplitudes generally coincident with the surface pressure wave; however, these plots are restrictive and can be challenging to associate directly with the wave fronts propagating from the Tonga eruption.

Looking at Figures 2A and 3A-B, we can begin to characterize some of the wave structures emanating from the Tonga eruption. We first see an LSTID propagating radially at speeds of 950 ± 170 ms^{-1}, with a wavelength > 1600 km, before slowing substantially to 600 ± 30 ms^{-1}after reaching ~2300 km range (Figure 3B). The trailing edge of this LSTID had a speed of 710 ± 115 ms^{-1} before the break at ~2300 km range, where it slows to 550 ± 15 ms^{-1}. A second LSTID with wavelength of 1350 ± 100 km, then propagates from the eruption at 555 ± 45 ms^{-1} before similarly slowing substantially to 390 ± 15 ms^{-1} after ~2500km range. Changes in propagation speed with radial distance can be clearly seen in Figure 3A, where the slopes of LSTID leading/trailing edges abruptly decrease. These breaks in propagation speed can be inferred more directly in Figure 3C by looking at the implied origin times of the waves. LSTIDs within 2300 km of the eruption have origin times of ~15 and ~20 minutes after the eruption, respectively, while the portions of the LSTIDs beyond 2300 km have implied origin times either coincident with the eruption or prior to it, depending on the velocity estimation method. A 15-minute delay is consistent with the time it would take an acoustic wave to propagate into the thermosphere, while there is no indication that LSTIDs were generated at the origin prior to the eruption. The speed of the later portions of the propagation of these TIDs are consistent with horizontally propagating thermospheric gravity waves (e.g. the direct wave) [Mayr et al., 2013].

Following these two LSTIDs, smaller MSTIDs are seen propagating from the eruption source region for up to six hours. The first of these MSTIDs propagates at a speed of 337 ± 17 ms^{-1} with an initiation time of 4:32 UT and corresponds almost perfectly with the propagation of a surface pressure wave associated with the eruption (Figure 2A). This first MSTID and the MSTID after it are clearly visible out to ranges of at least 16,000km and have wavelengths of 300 to 350 km. Secondary MSTIDs with wavelengths ranging from 250 to 500 km are also seen generated up to six hours after the passing of the initial pressure disturbance. These secondary MSTIDs have speeds that range from 200 to 400 ms^{-1}, with most of the later MSTIDs having speeds toward the lower end of that range, consistent with the characteristics of ducted AGW waves reflected between the Earth and the lower thermosphere [Mayr et al., 2013].

The behavior of the ionospheric response to this event appears very similar to that of the 2011 Tohoku earthquake, but without the initial Rayleigh Wave [Tsugawa et al., 2011]. Both events see initial LSTIDs with speeds near the ionospheric acoustic speed and subsequent MSTIDs with speeds near the surface acoustic speed.

One challenge with looking at the resulting disturbances in the manner shown in Figure 2A is that it assumes radial symmetry in the propagation of the TIDs. Many authors have noted preferential directional propagation of these structures associated with earthquakes [Inchin et al., 2020; Zettergren and Snively, 2019, for example]. It is likely that highly directional wave fronts may not be apparent in representations like Figure 2A, which assume isotropy. To get a clearer picture of the wave propagation without batching together all observed stations, in Figure 4 we generate analogous plots to Figure 3A but only for local regions with high GNSS station density. The boundaries of these regions are shown in Figure 1G. Using these plots, we can further examine the extent to which these waves propagate from the source.

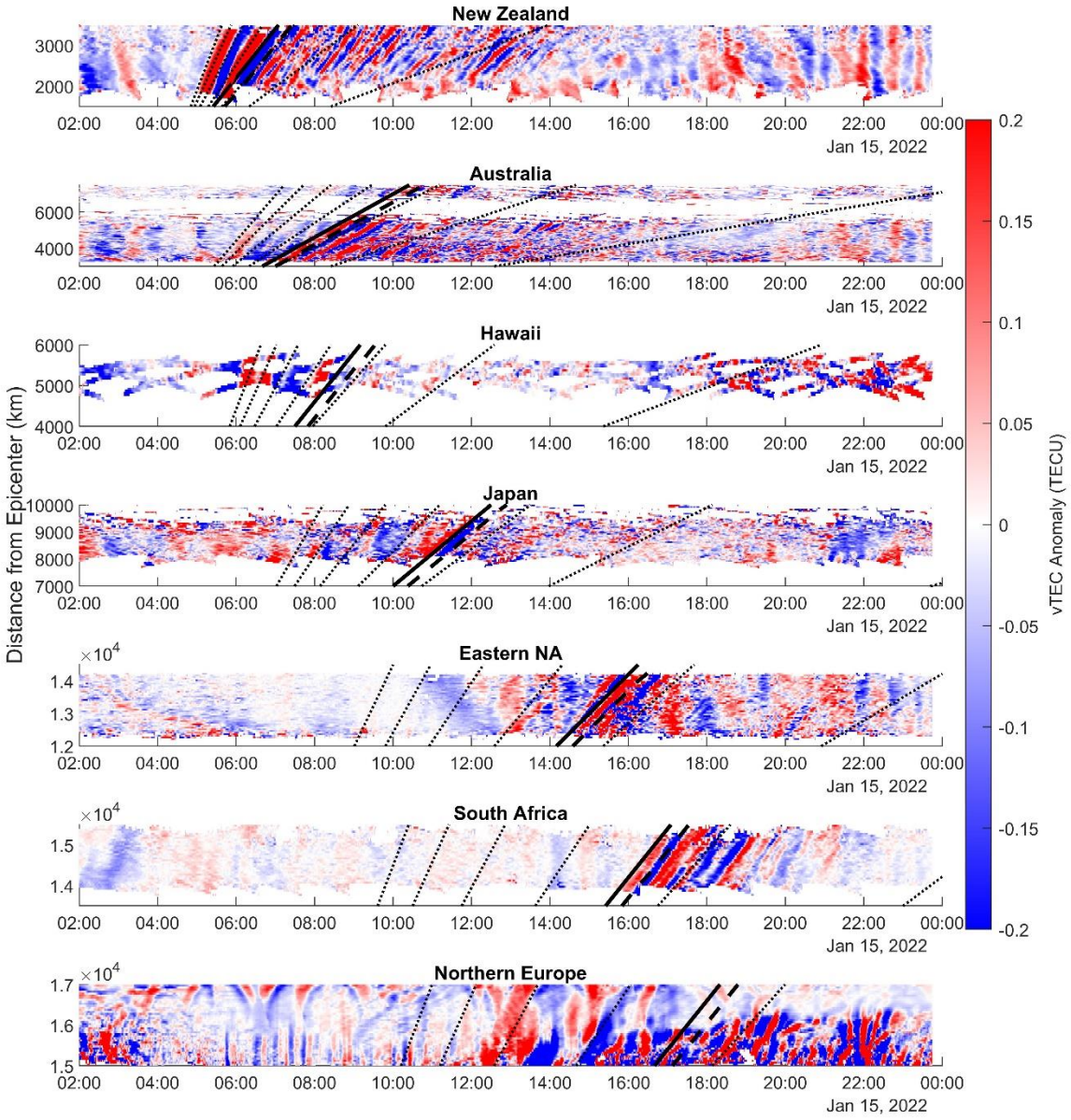

Figure 4*. vTEC anomalies plotted against distance from the epicenter for several sub-domain regions, demonstrated in Figure 1G.*

In Figure 4, we see the abundance of waves of various sizes in the region directly adjacent to the eruption (New Zealand), and we can more clearly track the propagation of

individual wave fronts. Interestingly, the LSTIDs do not appear to remain coherent in many other regions. Using the dotted propagation speed lines as reference, the first LSTID is seen clearly at New Zealand, Hawaii, and Northern Europe, with more inconclusive observation in Japan and Australia. Contrarily, the first LSTID is not apparent in South Africa and Eastern North America. Much of the same is seen for the second LSTID, but with a much clearer signature in Japan and a candidate signature in Eastern North America. Based on the geomagnetic location of the eruption and previous examinations of TIDs from similar sources, it is expected that waves will preferentially propagate along the magnetic field [Inchin et al., 2020; Zettergren and Snively, 2019]. With the eruption being in the southern magnetic hemisphere, this would imply preferential northward propagation of these waves. Similarly, the declination of the magnetic field would imply preferential propagation to the North East and South West, aligned with the magnetic field. Examining Figure 4 again, one may note that the fast LSTID structures are barely discernable in Australia, suggesting substantial attenuation of the waves to the West. These modes are completely absent in South Africa, which is roughly along the same propagation trajectory from the source as Australia. This suggests a substantial disinclination of LSTID propagation to the West from the eruption. In contrast, the first and second LSTID signatures are the dominant structures seen at Hawaii to the North East, near the geomagnetic conjugate point of the eruption site. Interestingly, while the first LSTID front at New Zealand appeared to rapidly slow after ~2300 km range from the source, we see strong LSTID signatures at Hawaii ahead of the 700 ms^{-1} marker and very close to where we would expect a 900 ms^{-1} wave, consistent with the initial LSTID phase speed seen in New Zealand. It appears from this that, while the LSTID slowed substantially as it propagated over New Zealand no such reduction in speed occurred to the North East at Hawaii.

The appearance of the first and second LSTIDs in Northern Europe, which is at similar magnetic declination to Tonga, is suggestive of highly preferential propagation directly due North of the eruption site; however, a lack of stations in that direction over the Pacific, outside of the auroral oval, makes any conclusions regarding the appearance of the LSTIDs in Northern Europe challenging to assert. The strong presence of the LSTIDs at Hawaii is suggestive; however, more data is necessary. Further conclusions regarding the appearance of these LSTIDs in Northern Europe will thus have to await measurements from alternative sources, such as radio occultation.

Subsequent MSTIDs originating from the eruption are seen at five of the seven test locations and arrive at times similar to the modeled atmospheric pressure disturbance. These waves are entirely consistent with AGWs generated from the propagating surface perturbation. The MSTIDs propagating from this disturbance form the dominant global ionospheric wave response from this event, with clear signatures at nearly all sampled GNSS locations. In Northern Europe, MSTID wave signatures of eruption origin are far less obvious, likely due to interaction with waves of auroral origin and the sheer distance from the eruption location; furthermore, at Hawaii the MSTIDs are barely discernable. The lack of clear MSTID signatures at Hawaii may be a product of the lack of stations in that area; however, the observed amplitudes after the passage of the surface pressure anomaly are considerably weaker than the LSTID structures ahead of the surface pressure anomaly, which is only matched at New Zealand. Given that Hawaii is very near to the eruption geomagnetic conjugate point, it is possible that conjugate TID structures, generated by electric field perturbations associated with the TIDs at the eruption location, are interfering with TIDs propagating directly from the eruption [Zettergren and

Snively, 2019]. This, however, cannot explain why the LSTIDs do not suffer similar interference problems.

Conclusions

Perhaps the most striking feature of this event is the generation of an initial LSTID with a phase speed of > 900 ms^{-1}. This wave is generated almost immediately after the event at nearly triple the surface acoustic speed and is close to the acoustic speed at the F-Region peak. This LSTID is shown to rapidly slow to propagation speeds near 700 ms^{-1} after propagating ~2300 km from the eruption location in the direction of New Zealand but did not exhibit such a reduction in speed at Hawaii, at even further ranges. Whilst the wave is a dominant structure in the vicinity of the eruption location, it appears to quickly dissipate depending on the direction of travel, where it is only barely discernable at Australia 4,000 – 6,000 km to the West of the eruption but forms the dominant wave response at Hawaii at similar ranges to the North East. Interestingly, the structure also seems to appear in Northern Europe between 12:00 UT and 13:00 UT, nearly directly due North from the eruption location. The initial LSTIDs generated from this event are likely acoustic waves generated from the initial eruption shock, while subsequent MSTIDs, propagating near the surface acoustic speed, correspond to AGWs generated by the subsequent atmospheric disturbance and persist to be generated up to six hours after the eruption. While the shock-related LSTIDs demonstrate strong directionality and attenuate much faster than the MSTIDs, the MSTIDs exhibit no clear directional preference and form the dominant wave response seen globally except near the eruption conjugate point where these MSTIDs are much less dominant. Future work will need to combine modeling with additional measurements from

radio occultation and of stratospheric/mesospheric winds to further elucidate the mechanisms at play.

Acknowledgements

We are grateful to the Australian Bureau of Meteorology, Space Weather Services for the provision of GNSS data. We acknowledge the New Zealand GeoNet project and its sponsors EQC, GNS Science and LINZ, for providing data/images used in this study. CDDIS is one of the Earth Observing System Data and Information System (EOSDIS) Distributed Active Archive Centers (DAACs), part of the NASA Earth Science Data and Information System (ESDIS) project. Datasets and related data products and services are provided by CDDIS, managed by the NASA ESDIS project. This material is based on services provided by the GAGE Facility, operated by UNAVCO, Inc., with support from the National Science Foundation and the National Aeronautics and Space Administration under NSF Cooperative Agreement EAR-1724794. A. McCaffrey and B. Reid are supported under Canadian Space Agency grant 21SUSTCHAI. Sean Elvidge is supported by the UK Space Weather Instrumentation, Measurement, Modelling and Risk (SWIMMR) Programme, National Environmental Research Council (NERC) grants NE/V002643/1 and NE/V002708/1.

Availability Statement

GNSS data for this study were provided by the following organizations: International GNSS Service (IGS), UNAVCO (https://www.unavco.org/data/gps-gnss/gps-gnss.html), Dutch

Permanent GNSS Array (http://gnss1.tudelft.nl/dpga/rinex), Can-Net (https://www.can-net.ca/), Scripps Orbit and Permanent Array Center (Garner, http://garner.ucsd.edu/pub/), French Institut Geographique National, Geodetic Data Archiving Facility (GeoDAF, http://geodaf.mt.asi.it/index.html), Crustal Dynamics Data Information System (CDDIS, https://cddis.nasa.gov/archive/gnss/data/daily/), National Geodetic Survey (https://geodesy.noaa.gov/corsdata/), Instituto Brasileiro de Geografia e Estatistica (http://geoftp.ibge.gov.br/informacoes_sobre_posicionamento_geodesico/rbmc/dados/), Instituto Tecnologico Agrario de Castilla y Leon (ITACyL, ftp://ftp.itacyl.es/RINEX/), TrigNet South Africa (ftp://ftp.trignet.co.za), The Western Canada Deformation Array (WCDA, ftp://wcda.pgc.nrcan.gc.ca/pub/gpsdata/rinex), Canadian High Arctic Ionospheric Network (CHAIN, http://chain.physics.unb.ca/chain/pages/data_download), Pacific Northwest Geodetic Array (PANGA, http://www.geodesy.cwu.edu/pub/data/), Centro di Ricerche Sismologiche, Système d'Observation du Niveau des Eaux Littorales (SONEL, ftp://ftp.sonel.org/gps/data), INGV - Rete Integrata Nazionale GPS (RING, http://ring.gm.ingv.it/),RENAG : REseau NAtional GPS permanent (http://rgp.ign.fr/DONNEES/diffusion/), Australian Space Weather Services (https://downloads.sws.bom.gov.au/wdc/gnss/data/),GeoNet New Zealand (https://www.geonet.org.nz/data/types/geodetic), National Land Survey Finland (NLS, https://www.maanmittauslaitos.fi/en/maps-and-spatial-data/positioning-services/rinex-palvelu), SWEPOS Sweden (https://swepos.lantmateriet.se/), Norwegian Mapping Authority (Kartverket, https://ftp.statkart.no/), Geoscience Australia (http://www.ga.gov.au/scientific-topics/positioning-navigation/geodesy/gnss-networks/data-and-site-logs), Institute of Geodynamics, National Observatory of Athens (https://www.gein.noa.gr/services/GPSData/),and European Permanent GNSS Network (EUREF,

https://www.epncb.oma.be/_networkdata/data_access/dailyandhourly/datacentres.php).

Barotropic TIGAR model simulation output for this study is available at https://doi.org/10.5281/zenodo.5933393.

References

Cervera, M. A., and Harris, T. J. (2014), Modeling ionospheric disturbance features in quasi-vertically incident ionograms using 3-D magnetoionic ray tracing and atmospheric gravity waves, J. Geophys. Res. Space Physics, 119, 431– 440, doi:10.1002/2013JA019247.

Chen, P., Y. Yao, & W. Yao (2017). On the coseismic ionospheric disturbances after the Nepal Mw7.8 earthquake on April 25, 2015 using GNSS observations. Advances in Space Research, 59(1), 103-113. https://doi.org/10.1016/j.asr.2016.09.021

Chou, M.Y., C. H. Lin, J. Yue, L. C. Chang, H.F. Tsai, and C.H. Chen (2017), Medium-scale traveling ionospheric disturbances triggered by Super Typhoon Nepartak (2016), Geophys. Res.Lett.,44, 7569–7577, doi:10.1002/2017GL073961.

Coster, A. J., Goncharenko, L., Zhang, S.-R., Erickson, P. J., Rideout, W., & Vierinen, J. (2017). GNSS observations of ionospheric variations during the 21 August 2017 solar eclipse. Geophysical Research Letters, 44, 12,041– 12,048. https://doi.org/10.1002/2017GL075774

Dautermann, T., E. Calais, and G. S. Mattioli (2009), Global Positioning System detection and energy estimation of theionospheric wave caused by the 13 July 2003 explosion of the Soufriere Hills Volcano, Montserrat, J. Geophys. Res.,114, B02202, doi:10.1029/2008JB005722

414 Heki, K. (2006), Explosion energy of the 2004 eruption of the Asama Volcano, central Japan,
415 inferred from ionospheric disturbances, Geophys. Res. Lett., 33, L14303,
416 doi:10.1029/2006GL026249.

417 Inchin, P. A., Snively, J. B., Zettergren, M. D., Komjathy, A., Verkhoglyadova, O. P., & Tulasi
418 Ram, S. (2020). Modeling of ionospheric responses to atmospheric acoustic and gravity
419 waves driven by the 2015 Nepal Gorkha earthquake. Journal of Geophysical Research: Space
420 Physics, 125, e2019JA027200. https://doi.org/10.1029/2019JA027200

421 Komjathy, A., Galvan, D.A., Stephens, P., et al. Detecting ionospheric TEC perturbations caused
422 by natural hazards using a global network of GPS receivers: The Tohoku case study. Earth
423 Planet Sp 64, 24 (2012). https://doi.org/10.5047/eps.2012.08.003

424 Komjathy, A., Yang, Y.-M., Meng, X., Verkhoglyadova, O., Mannucci, A. J., and Langley, R. B.
425 (2016), Review and perspectives: Understanding natural-hazards-generated ionospheric
426 perturbations using GPS measurements and coupled modeling, Radio Sci., 51, 951– 961,
427 doi:10.1002/2015RS005910.

428 Ma G, & Maruyama T (2003) Derivation of TEC and estimation of instrumental biases from
429 GEONET in Japan. Ann Geophys 21:2083–2093

430 Mayr, H.G., Harris, I., Varosi, F., Herrero, F.A., 1984a. Global excitation of wave phenomena in
431 a dissipative multiconstituent medium 1. Transfer function of the Earth's thermosphere. J.
432 Geophys. Res. 89, 10929–10959.

433 Mayr, H.G., Harris, I., Varosi, F., Herrero, F.A., 1984b. Global excitation of wave phenomena in
434 a dissipative multiconstituent medium 2. Impulsive perturbations in the Earth's thermosphere.
435 J. Geophys. Res. 89, 10961–10986.

436 Mayr, H.G., E.R. Talaat, & B.C. Wolven (2013). Global propagation of gravity waves generated
437 with the whole atmosphere transfer function model, Journal of Atmospheric and Solar-
438 Terrestrial Physics, 104, 7-17, https://doi.org/10.1016/j.jastp.2013.08.001

439 Nishioka, M., Tsugawa, T., Kubota, M., and Ishii, M. (2013), Concentric waves and short-period
440 oscillations observed in the ionosphere after the 2013 Moore EF5 tornado, Geophys. Res.
441 Lett., 40, 5581– 5586, doi:10.1002/2013GL057963

442 Savastano, G., Komjathy, A., Verkhoglyadova, O. et al. Real-Time Detection of Tsunami
443 Ionospheric Disturbances with a Stand-Alone GNSS Receiver: A Preliminary Feasibility
444 Demonstration. Sci Rep 7, 46607 (2017). https://doi.org/10.1038/srep46607

445 Themens, D.R., P.T. Jayachandran, R.B. Langley, J.W. MacDougall, and M.J. Nicolls (2013).
446 Determining Receiver Biases in GPS-derived Total Electron Content in Auroral Oval and
447 Polar Cap Region Using Ionosonde Measurements. GPS Solutions, 17(3), pp. 357-369, doi:
448 10.1007/s10291-012-0284-6

449 Themens, D. R., P.T. Jayachandran, M.J. Nicolls, and J.W. MacDougall (2014), A top to bottom
450 evaluation of IRI 2007 within the polar cap, J. Geophys. Res. Space Physics, 119, 6689–
451 6703, doi:10.1002/2014JA020052.

452 Tsugawa, T., Saito, A., Otsuka, Y. et al. (2011). Ionospheric disturbances detected by GPS total
453 electron content observation after the 2011 off the Pacific coast of Tohoku Earthquake. Earth
454 Planet Sp 63, 66. https://doi.org/10.5047/eps.2011.06.035

455 Vasylkevych, S, Žagar, N. A high-accuracy global prognostic model for the simulation of
456 Rossby and gravity wave dynamics. Q J R Meteorol Soc. 2021; 1989– 2007.
457 https://doi.org/10.1002/qj.4006

458 Watson, C., Jayachandran, P. T., Spanswick, E., Donovan, E. F., and Danskin, D. W. (2011),
459 GPS TEC technique for observation of the evolution of substorm particle precipitation, J.
460 Geophys. Res., 116, A00I90, doi:10.1029/2010JA015732.

461 Watson, C., Jayachandran, P. T., Singer, H. J., Redmon, R. J., and Danskin, D. (2015), Large-
462 amplitude GPS TEC variations associated with Pc5–6 magnetic field variations observed on
463 the ground and at geosynchronous orbit, J. Geophys. Res. Space Physics, 120, 7798– 7821,
464 doi:10.1002/2015JA021517.

465 Zawdie, K. A., Drob, D. P., Huba, J. D., and Coker, C. (2016), Effect of time-dependent 3-D
466 electron density gradients on high angle of incidence HF radiowave propagation, Radio Sci.,
467 51, 1131– 1141, doi:10.1002/2015RS005843.

468 Zettergren, M. D., & Snively, J. B. (2019). Latitude and longitude dependence of ionospheric
469 TEC and magnetic perturbations from infrasonic-acoustic waves generated by strong seismic
470 events. Geophysical Research Letters, 46, 1132– 1140.
471 https://doi.org/10.1029/2018GL081569

472 Zhang, S.-R., Erickson, P. J., Coster, A. J., Rideout, W., Vierinen, J., Jonah, O. F., &
473 Goncharenko, L. P. (2019). Subauroral and polar traveling ionospheric disturbances during
474 the 7–9 September 2017 storms. Space Weather, 17, 1748– 1764.
475 https://doi.org/10.1029/2019SW002325

476

477

478